Shock tube radiation measurement in expanding air flows.

Augustin Tibère-Inglesse[1], Khalil Bensassi[2], Aaron M. Brandis[2], Brett A. Cruden[2]
[1] NASA Postdoctoral Program Fellow at NASA Ames Research Center, Mountain View, CA, 94035, USA
[2]AMA Inc at NASA Ames Research Center, Mountain View, CA, 94035, USA

1. Introduction

During atmospheric reentry, such as for Mars or lunar return, a capsule enters the atmosphere at velocities that can exceed 10 km/s. The strong shockwave that forms in front of the capsule heats the gas up to temperatures around 10,000K. The high temperature of the gas leads to ionization, molecular dissociation, excitation and radiation being significant to the total heat flux [1] [2]. The study of the radiative and convective heat transfer of such a plasma is critical for the design of the entry capsule thermal protection system (TPS). The predicted heat flux on the forebody of the vehicle during reentry was the focus of past research and is relatively well understood now [3] [4], typically uncertainties on radiative heat fluxes are approximately 30% for entry velocities between 10 to 15 km/s. The uncertainty tends to be higher for conditions corresponding to larger degrees of non-equilibrium, i.e. lower speeds and lower density. In the afterbody region, the uncertainties on the predicted heat fluxes are much higher. Comparison between simulations and measurements performed using radiometers on the back shell of the FIRE II mission showed disagreement up to 100% on some regions in the afterbody [5]. These high uncertainties/errors come from two primary physical phenomena that take place in the afterbody region. The first is the presence of significant quantities of carbon in the plasma, introduced via the ablative heat shield in front of the capsule. The second is the hydrodynamic expansion of the plasma as it passes over the capsule shoulder from the forebody to the afterbody region. This expansion rapidly cools the plasma, forces plasma recombination, and can lead to a departure from chemical equilibrium. This chemical nonequilibrium and the resulting radiation, dominated by atomic nitrogen radiation emitting in the VUV, are not accurately modeled at the moment [5]. Due to the lack of ground experiments looking at the afterbody region, high uncertainties remain on modeling these two phenomena and, consequently, the total radiative heat flux. Measurements were performed in a shock tube to look at the radiation in an expanding flow over a wedge in an attempt to provide data for validating models [6]. Recent experiments [7] [8] were made in a plasma torch facility to measure the radiation of such a recombining plasma, but no other data are available for condition more closely replicating flight.

The EAST facility has been widely used in the past to provide experimental data aiming to validate radiative heating models [9] [10]. However, all the past studies involved measurements of compressing flows. In order to study recombining flows, an expansion cone was installed in the EAST facility, downstream of the standard test section. This paper presents results of the experimental campaign performed using this cone

to spectrally image expanding shocked gas flow. Two targeted velocities were chosen for these tests, 10 and 11 km/s at the cone entrance, being representative of a lunar return mission. Four spectrometers are mounted at one axial position of the cone to measure the radiation during expansion. Quantitative data from optical emission spectroscopy are used to infer the radiating species concentrations [11]. Computational Fluid Dynamics (CFD) simulations were also performed to provide insight into physical properties that are not possible to measure and compare with experimental data.

2. Experimental setup

The Electric Arc Shock Tube (EAST) facility has been described in detail in previous publications [12] [13] [14], with a brief description provided here. This facility is composed of a 1.2 MJ, 1.3mF capacitor bank that drives a 10.16 cm aluminum shock tube. A schematic of the EAST facility is presented in Figure 1. Section 3 results will show that the test time for this test campaign was particularly important and needed to be higher than previous test series looking only at compressing flows. In an effort to increase the test time, different configurations were investigated. An optional 3-meters long helium or helium/argon mixture buffer can be added between the driver and the shock tube which is separated from the rest of the tube with either a 0.003" aluminum, a 0.0005'' Kapton or 3 μm aluminized polyester diaphragm. Tests were performed using a 11-inch conical driver [15] that has been the facility standard for several decades, as well as a 30-inch cylindrical driver employed in studies in the 1960's [16] [17] and the 1980's [13]. Diaphragms made of thin (0.003") unscored aluminum sheet and thick (0.12") scored stainless steel are employed in different tests. An expansion cone was installed immediately following the driven section, 12.5 m from the primary diaphragm. A second mylar diaphragm isolating the cone exit from the dump tank is broken by the shock after the experimental measurements are collected. The expansion cone has a 10-degree half-angle, beginning at 10.16 cm diameter and expanding to 76.2 cm over its 1.9 m length. There are three pairs of rectangular ports along the axial axis of the cone at 28.9, 77.1, 128 cm but only the first one is instrumented with four spectrometers imaging different wavelength regions: one in the Vacuum Ultraviolet (VUV), one in the UV/visible, one in the visible/near-infrared and one in the mid infrared. This optical instrumentation is similar to that described in Refs [12] [14]. These spectrometers will be labeled as VUV, Blue, Visible and IR. Calibrated light sources are used to perform calibration from pixel counts to absolute intensities [14]. The calibrated spectra are then analyzed using the NEQAIR radiation code [11] [18] to get temperatures and species density measurements [19]. The shock velocity in the tube is determined using the shock position versus time measured using piezoelectric gauges (PCB 132A) mounted along the axis of the tube which is then extrapolated to the cone entrance. A pitot rake was also installed 51.7 cm from the cone entrance. The shock velocity in the camera location is estimated using the shock position versus time at 6 cm and 43 cm from the cone entrance, determined using a PCB or the pitot rake, respectively.

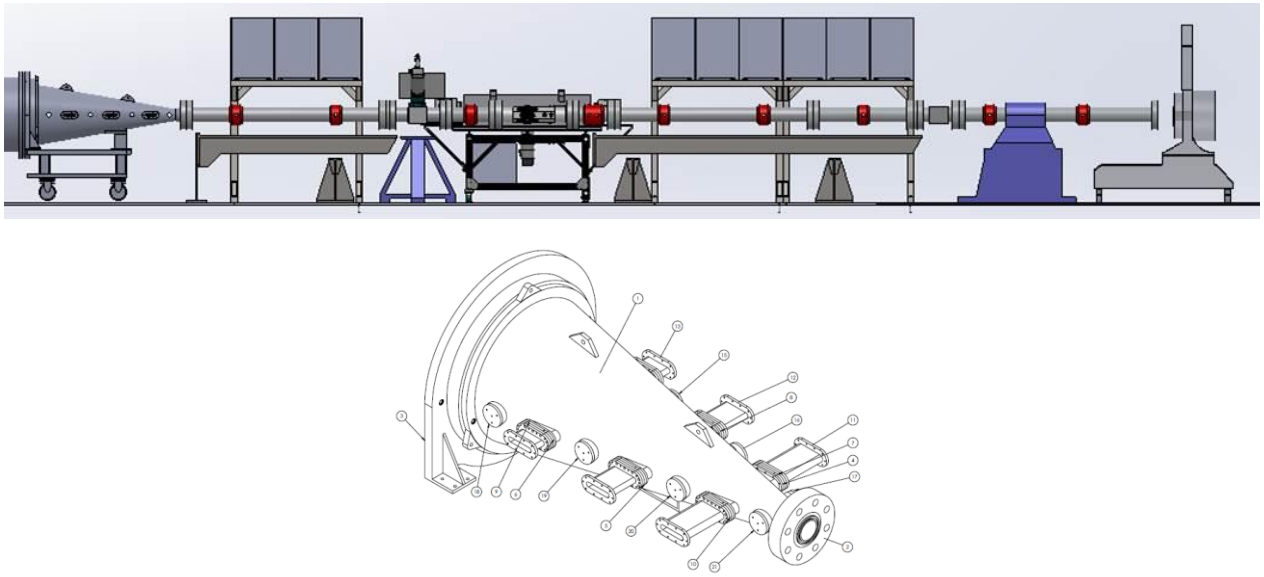

Figure 1: Top: schematic of the EAST facility (shock travels from right to left). An expansion cone (bottom) was added to the end of the driven section.

The EAST testing conditions at the entrance of the cone for this experimental campaign, known as Test 63, are shown in Figure 2. Free-stream conditions of past or planned missions are also shown for comparison. The level of gas expansion around to the backshell will vary from mission to mission and also when compared to the test. Test 63 targeted nominal velocities of 10 km/s and 11 km/s at a free stream pressure of 0.2 Torr which are representative of a lunar return. Variability from the target test conditions is observed due to the randomness of the arc conditions and attenuation of the shock as it traverses the tube. The test gas considered is always pure air, including some impurities as discussed in the results section.

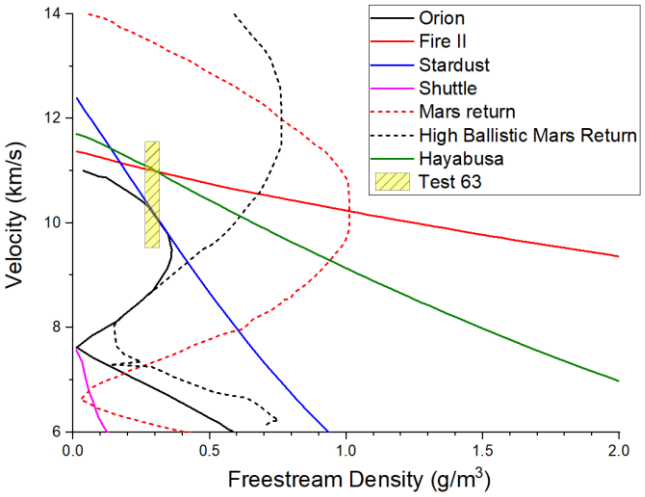

Figure 2: Comparison between past (solid lines) and future (dashed) missions and EAST test 63 conditions.

3. CFD simulations

In order to interpret and better understand experimental results, CFD simulations of the EAST expansion cone, were made. The simulations aimed to reproduce shot 8 of the test campaign which represents the 10 km/s targeted velocity. The CFD tool that is used in this simulation is COOLFLuiD [20] The estimated velocity at the cone entrance for this shot was 10.2 km/s which represents the input for the simulation. The computational approach is briefly described here. The system of coupled partial differential equations are discretized using the finite volume method. The convective fluxes are computed using the AUSM$^+$ scheme [21]. In order to get second order accuracy, each one of the cells centered state variables is linearly extrapolated to the face quadrature points. The linearly reconstructed state variables are calculated using a least-squares method. In order to prevent the appearance of oscillations near discontinuities, a flux limiter is needed for the reconstructed states. In the present work, Venkatakrishnan's limiter [22] is used. The second order time accurate Crank-Nicolson scheme is used for time accurate simulation. At each time step, the resulting linear system is solved implicitly using a Newton method. The latter requires a matrix inversion which is generally achieved by approximate methods. We use the Generalized Minimum RESidual (GMRES) algorithm, complemented with an Additive Schwartz pre-conditioner provided by the PETSc library [23] [24]. All simulations assumed a 2D axisymmetric flow. Two different grids, named with or without a window, were used to study the impact of the window used at the spectrometer location on the flow (see Figure 3). As shown in Figure 1, the cone section at the spectrometer location is not axisymmetric and the 2D axisymmetric simulations effectively means a 360° window, which is over-estimating the influence the window has on the flow.

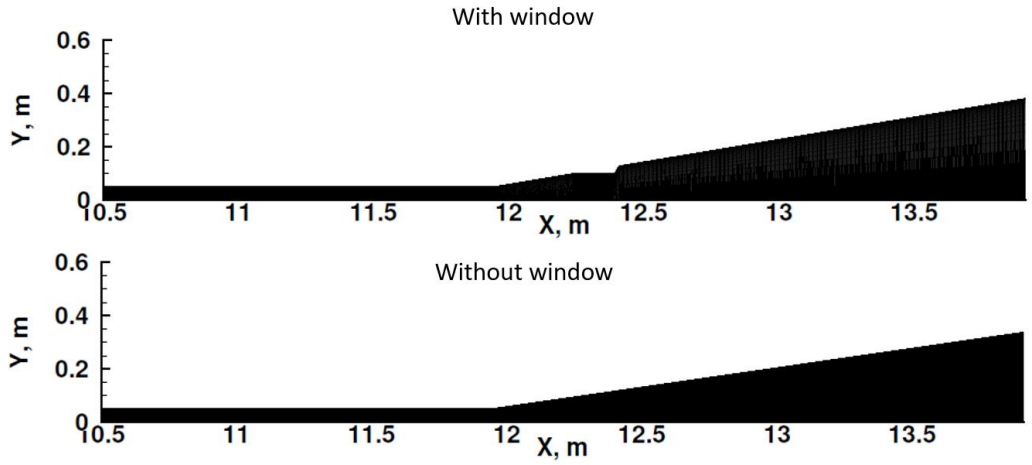

Figure 3: The two different grids used for the simulation labeled "With window' (Top) and "Without window" (bottom).

Results of the temperature contours are presented for both simulations and are presented in Figure 4. The main features expected in the cone are the curved transmitted shock, which is the compression of freestream gases in the cone, followed by an expanding flow that consists of gases originating from the incident shock generated in the shock tube. It is this latter part that is of interest to the radiation of expanding flows. The measured radiation will correspond to the total radiation along the line of sight. Figure 4 shows that the

line of sight, located a few centimeters after the shock front, comprises a hot pocket of the compressed gas close to the wall and a colder pocket of the expanding flow in the center. The measured radiation will be a mix of radiation coming from the compressing and expanding gas. Based on these simulations, the interface between the compression and expansion region of the shock is approximately 6.5 cm from the shock front in both simulations. The two main differences between the simulation with or without windows is the presence of an oblique shock in the compression region in the case with the window and the shock front boundary layer shapes. The curvature of the shock without window is also slightly more severe than the one with the window. All these observations will be compared with experimental data in Section 4.

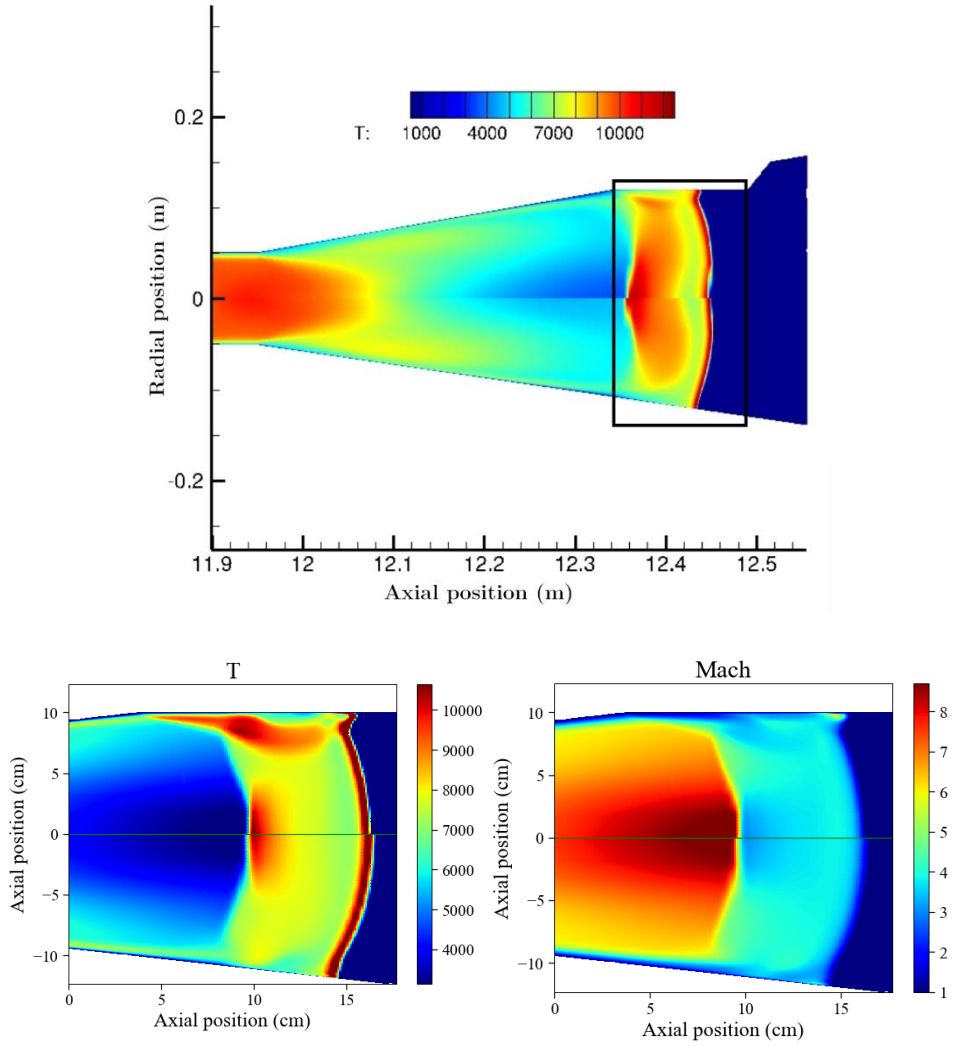

Figure 4: Top: Translational-rotational temperatures contour predicted by COOLFLuiD using the grid with the window (top) or without (bottom). The black square represents approximately the region measured by the spectrometers. Bottom: Contour of translational-rotational temperatures (left) and Mach number (right) over the spectrometer location.

To compare the fluid properties between the two CFD simulations and experiments, the wall pressure and pitot pressure measured 12.53 and 12.43 m from the primary diaphragm, respectively, was computed (See top of Figure 4 for the position). The former was measured using a PCB, while the latter was measured using the pitot rake. The comparison between measurements and simulations with or without window is given in Figure 5. The presented pitot pressure corresponds to the centerline pitot probe (named pitot 5). Because the two measured pressure points are located after the window, significative differences are observed between both simulations. The pitot pressure is relatively well predicted by the simulation performed with the window, while the simulation without the window underpredicts the pressure in the shock front. A similar trend is observed for the wall pressure, despite an overprediction of the pressure in the shock front; which is well predicted by the simulation performed without the window. However, after the shock front, that simulation overpredicts the wall pressure. While none of the two presented simulations is representative of the experimental configuration, it is clear that the window plays a major role in simulating the state of the gas and needs to be investigated more in the future. While these two simulations will be compared with experimental data as two bounding cases, it is unclear where within these bounds results of a 3D simulation will lie.

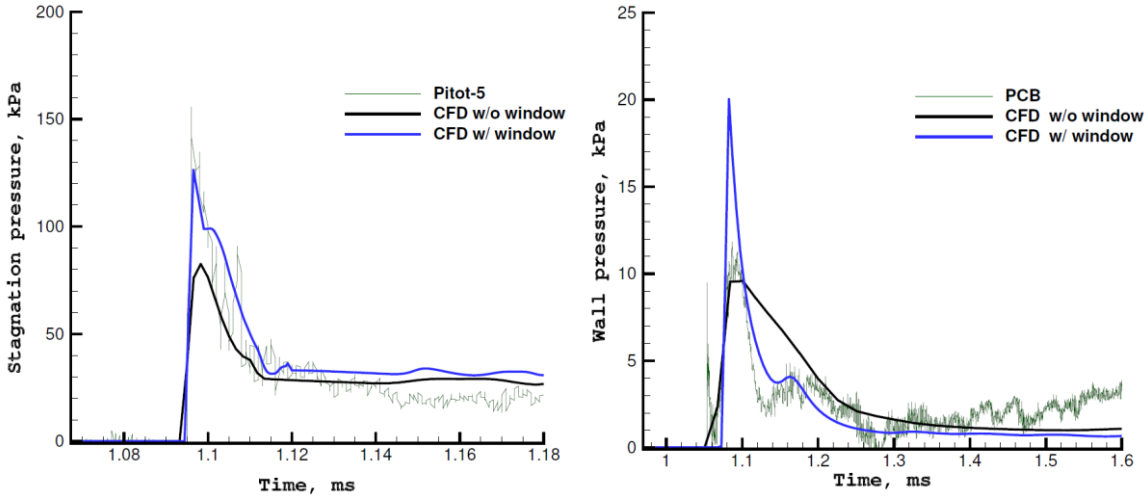

Figure 5: Comparison between simulations performed with (blue) or without (black) the window and measurements (green) for centerline pitot pressure (left) and wall pressure (right).

Finally, radial lines of sight were extracted from COOLFLuiD results and NEQAIR simulation performed to compute the radiance at discrete axial positions. The accumulated radiance, representing the sum of the radiance across the tube, integrated from 200 to 500 nm and the corresponding volumetric radiance are presented in Figure 6 for the simulation with the window. This wavelength range is representative of the radiance measured by the Blue camera. The total radiance profile represents the accumulated radiance measured by all four cameras. This profile presents a double peak in radiance which is believed to come from the curvature of the shock. Based on the volumetric radiance contour, the first peak radiance is attributed to the centerline shock front radiance while the second to the addition of the two-shock front and

boundary layers radiance at the wall. Behind the shock front, radiation from an oblique shock is also observed close to the wall, up to 8 cm after the shock front. As presented in Figure 4, the expansion region starts 6.5 cm after the shock front, and Figure 6 shows that the radiation of the lines of sight located after this point will be a combination of radiation coming from both compressing and expanding region.

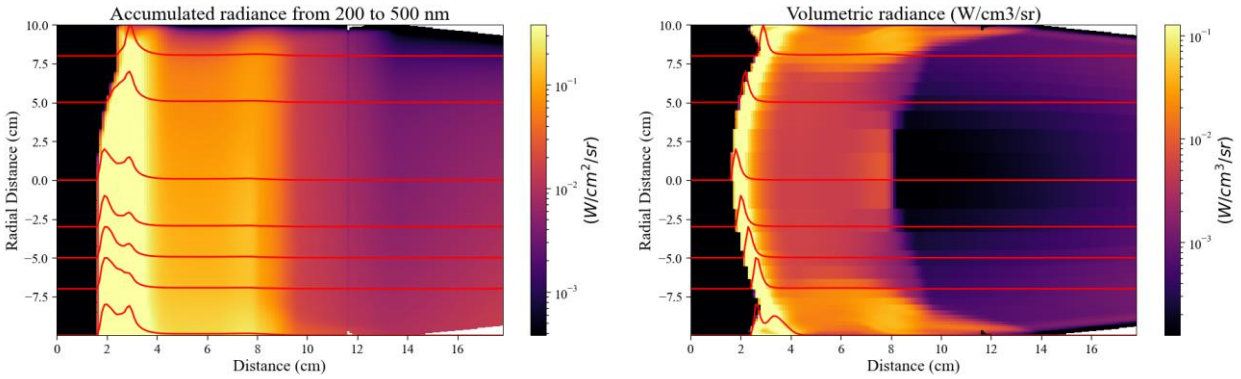

Figure 6: Accumulated (left) and volumetric (right) radiance computed using COOLFluiD and NEQAIR simulations.

Figure 6 provides an estimate of the test time which will be needed in the experiment to observe significant radiation from the expansion region. The contribution to the total radiation coming from the expanding flow is presented in Figure 7 for both simulations. This contribution over the 200-500 nm range becomes dominant 7 cm and 10.5 cm after the shock front for the simulations without or with the window, respectively. The shock velocity predicted by the simulations without and with the window is 6.49 and 6.97 km/s, respectively. Based on these results, the needed test time in the experiments to study expanding flow radiation should be at minimum between 10.8 to 15 μs. A wider wavelength range (145-900 nm) is also shown in Figure 7 and does not indicate need for a further increase in test time requirements.

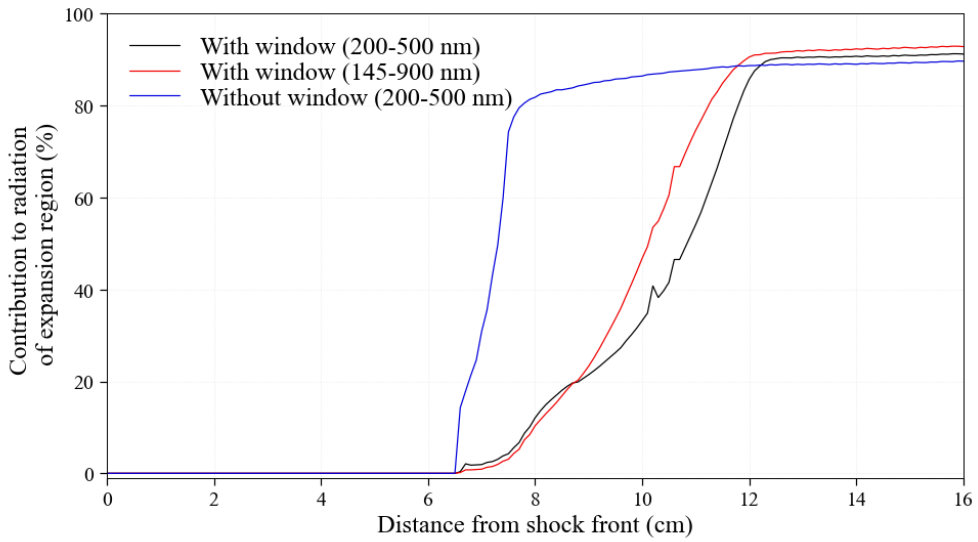

Figure 7: Contribution of the expanding region to the total simulated radiation (the shock front is located approximately at 1.5 cm)

Finally, the integrated radiance axial profiles which will be compared with experimental results are plotted in Figure 8. The 200-500 nm and 500-900 nm corresponds to the region measured by the Blue and Red camera, respectively, while the 145-900nm corresponds to the total significative radiation measured by all cameras. Overall, the main differences observed between the two simulations are the distance between the two emission peaks (higher in the simulation without a window), the ratio of the peak intensity (the second peak being more intense in the simulation with the window relatively to the first one) and overall radiation intensity (higher in the simulation with the window). The first difference is due to the shock curvature while the last one could be due to the slower velocity predicted for the simulation without the window, the test section diameter being higher at the position of the end of the window.

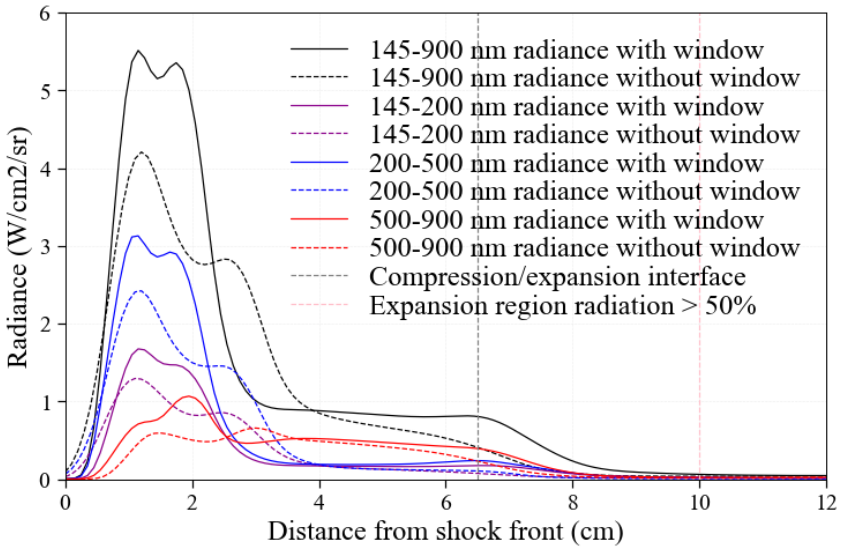

Figure 8: Radiance profiles with (solid lines) or without (dashed) the window for different wavelength regions.

4. Experimental results

As explained in section 3, the curvature of the shock explains the double peak radiance intensity ratio. It is important to correctly predict both the intensity ratio and distance between the two peaks. This curvature can be experimentally estimated using the time of arrival of the shock front on the different pitot probes. A comparison of the four shots highlighted in Table 1 with both simulations is presented in Figure 9. The curvature of the shock front is relatively consistent across the 4 experiments. The slight differences observed for shot 36 is attributed to a lower velocity at the cone location for this shot, due to a higher deceleration of the shock speed through the tube. The curvature of the shock seems relatively well predicted by CFD. Note however that the location of the shock front in the CFD simulations is slightly different than the comparison made with experiments (12.46 vs 12.53 m from the primary diaphragm, respectively).

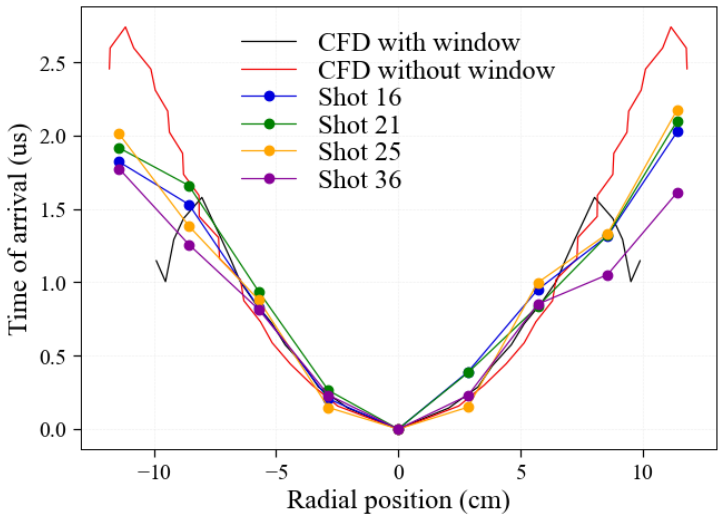

Figure 9: Comparison between the experimental and predicted shock front time of arrival on the pitot probes for different shots and both COOLFluiD simulations.

An example of the experimental spectral images obtained from test 63 for the Blue camera is presented in Figure 10. The complete dataset of measurements contained data from the four cameras. For each camera, the data are spectrally and spatially resolved, giving a 3D map of radiance versus these two variables. Horizontal and vertical slices shown in Figure 10 represent the integrated radiance over the spectral and the spatial variable, respectively. The horizontal slices can be used to estimate the shock front location and to be compared with the predicted radiance presented in Figure 8. The two experimental spectra presented in Figure 10 represents two typical shots observed through the test 63 campaign. Shot 22 presents strong lines around 6 cm which are attributed mainly to metallic species (mainly Fe) and other impurities from stainless steel. Therefore, the arrival of these lines is attributed to the arrival of the driver gas. Using the estimated measured velocity at the camera location, these strongly contaminated shots allow to get a clear estimation of the test time. However, these shots usually have a relatively small test time. Shot 21 on the other hand, represents a case where no strong metallic lines are observed in the Blue camera despite using a stainless-steel primary diaphragm. There is however faint Ca^+ lines (at around 393 and 396 nm) visible starting around 9 cm. On other weakly contaminated shots like shot 21, faint Al lines may become visible before Ca^+ lines. In that case, the test time is harder to define as both Ca and Al are not species present in stainless steel. As a first approximation, the arrival of these faint lines will be used to estimate the test time, which is expected to give a lower bound of the real test time. While the real test time may be higher, additional analysis or measurements may be needed to determine it accurately. No significant radiation from impurities is observed in the Red camera behind the shock except for an hydrogen line which is believed to come from water vapor in the tube, making it not possible to determine the test time with the Red camera.

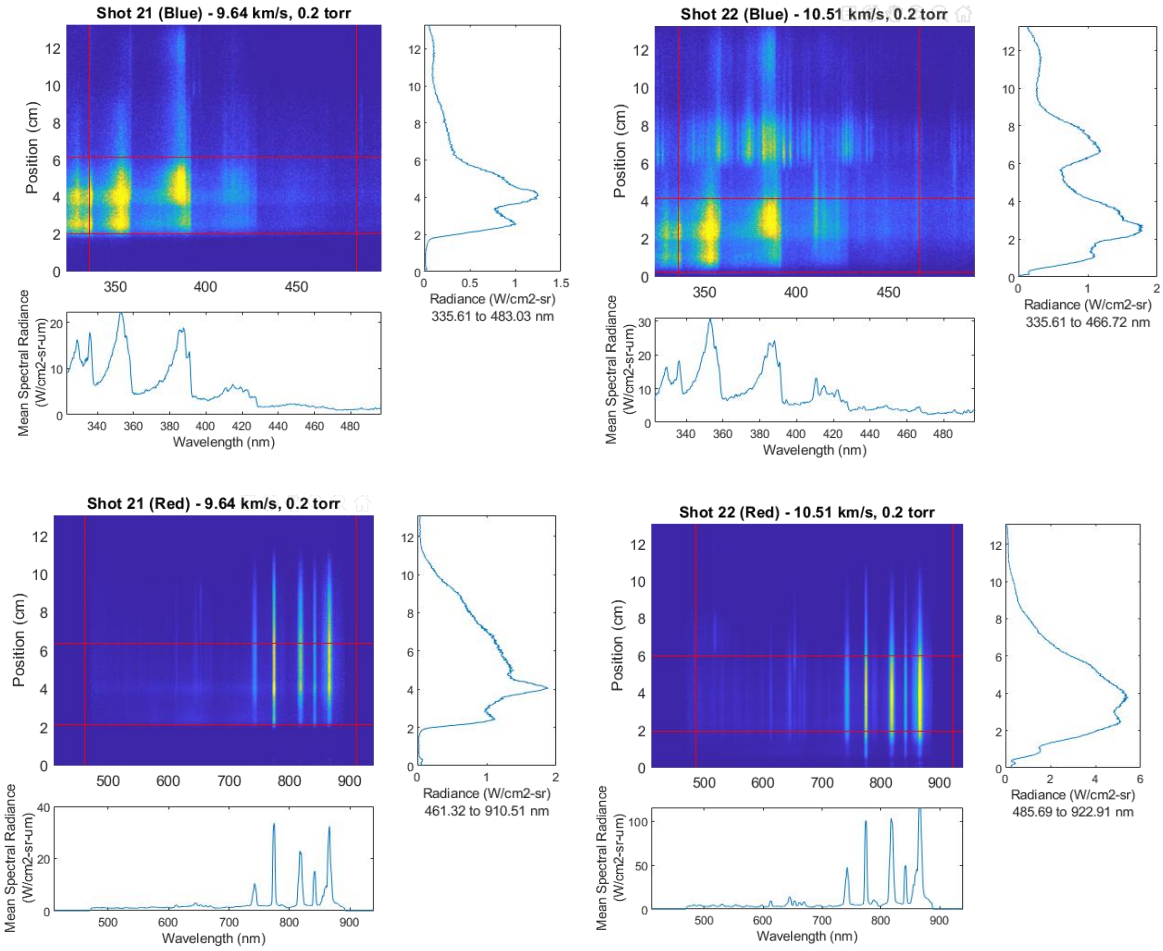

Figure 10: 3D spectral intensity maps obtained for shot 21 and 22 with the Blue (top) and Red (bottom) cameras

During test 63, 37 shots were performed but only about 50% have useable data for radiation study. Many of the early shots were performed without spectrometers on purpose to study other properties of the flow, like the achieved velocity, axisymmetric property of the flow... A shot is considered useable if both the shock speed and test time can be estimated. This definition discarded shots with experimental spectra and trace of arrival where the shock front was not measured by the camera, and therefore where the test time could not be estimated. Table 1 presents the summary of all useable shots for test 63. The reported test time in the table corresponds to the test time using the velocity at the camera location determined via the pitot probe closest the tube wall (pitot 1). The driver and buffer configuration are also given along with the wavelength ranges for each camera. The total spatial resolution, as presented in Figure 10, is about 13 cm, and the shock front is usually located around 2 cm. The velocity at the camera location for all shots is approximately 8 to 9 km/s, which leads to a maximum test time recorded by one camera of 12 to 14 us. Because of the weakly contaminated shots, like shot 21, the VUV center wavelength was set to the same as

the Blue camera. In these cases, the VUV camera was triggered 12 μs later than the Blue camera to measure radiation further downstream of the shock front and in the hope of measuring atomic lines originating from diaphragm species. However, these lines were never measured further away from the shock front and the test time was therefore only estimated using the arrival of the first impurity lines (Ca^+ or Al). Finally, four shots are highlighted in Table 1 and represent the highest quality data-sets, containing spectral measurements on multiple cameras, as well as a relatively high test time. The shock velocity at the camera location was estimated using the wall pressure measured by the PCB downstream closest to the test section, and a pitot probe of the pitot rake closest to the wall (pitot 1). An additional estimation of the shock velocity was also computed using the centerline pitot probe (pitot 5).

Table 1: Summary of exploitable shots available for test 63 campaign

Shot #	Velocity (km/s)		Camera wavelength range (nm)				Test time (us)	Driver (11'' conical or 30'' cylindrical)		Buffer
	Cone entrance	Camera location	VUV	Blue	Red	IR		11''	30''	
8	10.20	8.39		323-497			8.9	✓		
9	11.02	9.20		323-497			4.9	✓		
11	10.55	8.94		323-497	410-939		8.4	✓		
12	10.26	8.62	162-218	323-497	410-939		4.1	✓		
13	9.88	8.33	162-218	323-497	410-939		7.8	✓		
14	10.29	8.58	162-218	323-497	410-939	775-1407	8.2	✓		✓
16	**11.11**	**9.46**	**162-218**	**323-497**	**410-939**	**790-1423**	**8.5**		✓	
21	**9.64**	**8.18**	**298-522**	**323-497**	**410-939**		**9.2**		✓	
22	10.51	8.88	298-522	323-497	410-939		6.2		✓	
23	9.21	7.72	273-497	300-472	410-939		6.5		✓	
25	**10.24**	**8.35**	**273-497**	**298-472**	**410-939**		**9.0**		✓	
30	10.67	8.88	273-497	298-472	410-939		6.2	✓		
31	9.83	8.39	273-497	298-472	410-939	784-1417	8.3	✓		✓
32	9.78	8.42	273-497	298-472	410-939		3.6	✓		✓
33	9.47	8.19	273-497	298-472	410-939		5.5	✓		✓
36	**9.94**	**8.08**	**273-497**	**298-472**	**410-939**		**10.5**	✓		✓(He/Ar)

The integrated radiance profiles for the Blue and Red cameras of different shots are presented in Figure 11. Only the shots with an estimated test time of 8 μs or above are presented. The radiation measured by the Blue camera is dominated by molecules while the radiation measured by the Red camera is dominated by atoms, as observed in Figure 10. For the Blue camera, the radiance profiles between different shots with similar velocities are also relatively close when the intensity ratio of the two peaks and the distance between the two peaks is compared. For the Red camera, larger discrepancies in absolute intensities are observed behind the shock, while the intensity of the shock front seems relatively consistent from shot to shot. The temperature predicted by the CFD simulations behind the shock front is in the 7000-9000 K range where nitrogen dissociates. Therefore, a slight change in velocity and therefore, increase in post-shock temperature

can lead to a much higher atomic nitrogen concentration. This sensitivity in small differences in shock speed might be part of the reason for the variations in the observed radiance profiles. A comparison of the radiance profiles predicted by both simulations are also presented for the shots close in velocity to shot 8. Both simulations underpredict the measured radiance by the Blue camera. The NEQAIR simulations were performed assuming a Boltzmann distribution which should overpredict the nonequilibrium radiation region of the shock. However, the shock velocity in both simulations (6.49 and 6.97 km/s without or with the window, respectively) is significantly lower, more than 20%, than the experimental estimation (8.39 km/s) which could explain the global radiation underprediction. While two peaks in intensity are observed in both the simulations and experiments, the distance, and the ratio of these two peaks are not well captured. The intensity ratio of the two peaks are relatively well predicted by the simulation with the window while the distance between the two peaks is better predicted by the simulation without the window. As presented in Figure 9, the curvature of the shock is relatively well predicted. Therefore, the observed differences come from not yet modelled phenomena. The intensity of the second peak in the simulation with the window is higher due to the thickness of the boundary layer forming at the window. The experimental line of sight will be impacted by a similar boundary layer, explaining why the intensity of the ratio is better predicted with this simulation. On the other hand, this simulation also largely underestimates the experimental cone section surface at the camera location leading to an underestimation of the mean distance between the centerline shock front and the wall shock front. The velocity will also be largely impacted by the simulation. For these two reasons, the distance between the two peaks is believed to be better represented by the simulation without the window. A 3D simulation may be needed to confirm these conclusions. Further away from the shock front, the simulations still underpredict the measured radiation except when compared to shot 25, which measured radiation significantly lower than shots 8 and 14, even if the velocities of these shots were close (within 1%). Overall, the same comments apply to the radiance measured by the Red camera, with higher discrepancies in absolute intensities, which could be expected considering the strong intensity variation from shot to shot. The large increase in radiation measured by the Blue camera for shots 11 and 13 is attributed to the arrival of atomic lines originating from the primary diaphragm.

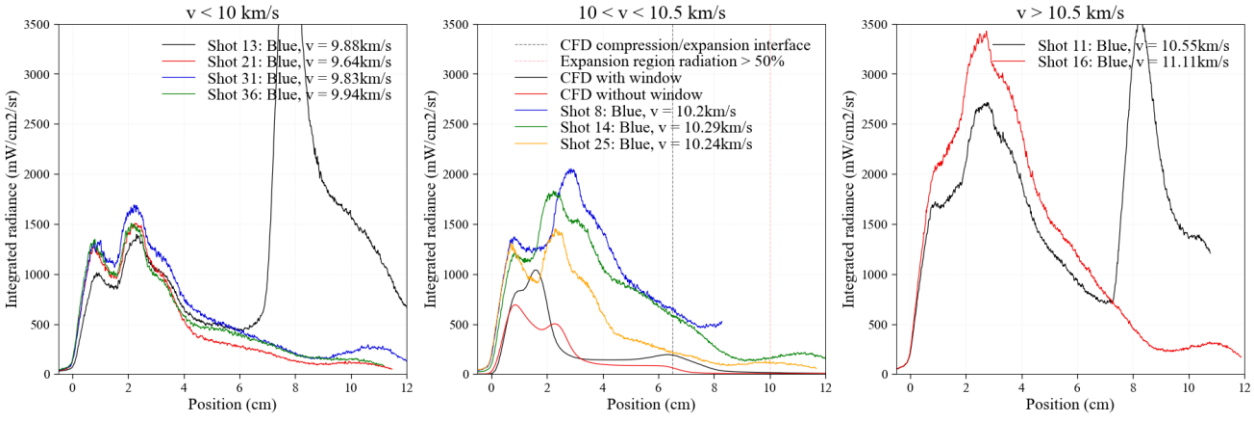

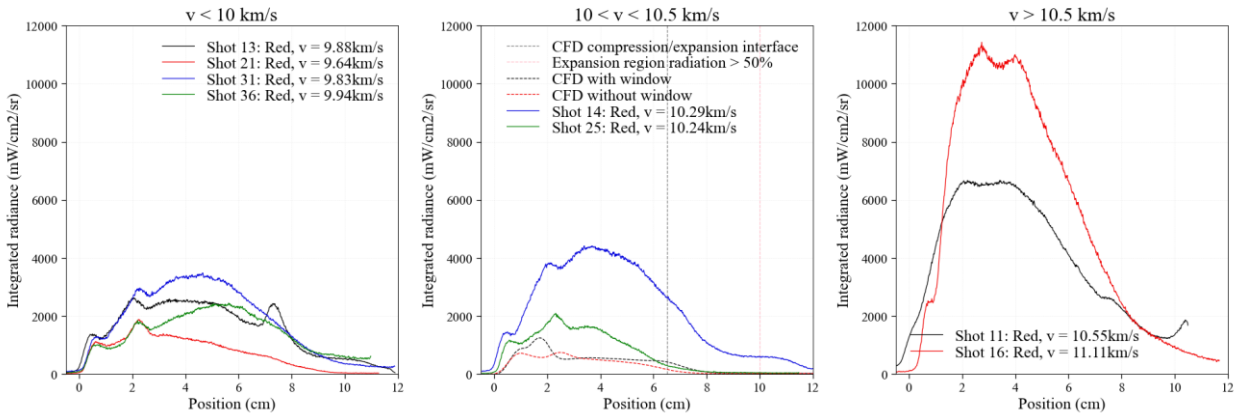

Figure 11: Comparison between the integrated radiance profile for different shots and simulations, for the Blue (top) and Red (bottom) cameras.

To further study the radiation measured by the Blue camera, an extended analysis was performed on shot 21. This shot was chosen as it represents the shot where the least radiation from impurities was observed. To study spatially resolved spectra, the radiance was binned, over 0.5 cm intervals before 5 cm, and 1 cm after, starting from the shock front (following a similar method presented in Ref. [19]). These intervals represent a compromise between the signal-to-noise ratio and spatial resolution. The contribution to the total radiation from individual species was extracted based on fitting the spectra with NEQAIR calculations. Results are presented in Figure 12. The two intensity peaks, corresponding to the centerline and wall shock front radiation, are mainly composed of N_2 and N_2^+ radiation which then decrease further away from the shock front. Only 2.2 cm from the shock front, significative radiation from the cyanogen radical (CN) is observed. Carbon is present as an impurity in the test and is believed to originate from the tube wall [12]. CN becomes the main radiator after 7 cm.

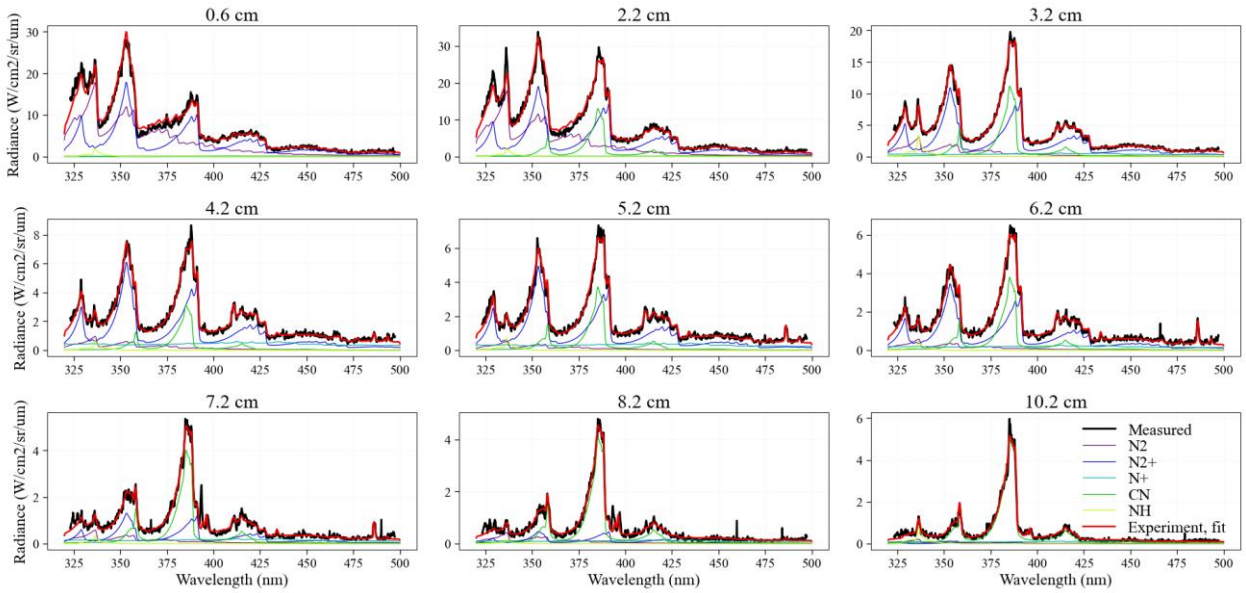

Figure 12: Experimental and fitted spectra using NEQAIR at different axial positions. 0.6 and 2.2 cm represents the centerline and wall shock front respectively.

As carbon was not included in simulations, CN radiation will not be predicted. The NEQAIR fitted spectra can be used as an estimate to remove radiation from all impurities. The resulting radiance profile is then compared to the CFD predictions in Figure 13. For the Blue camera, a better agreement between measurements and the simulation performed with a window in terms of the absolute intensity is observed. After 6 cm, the agreement becomes relatively good, around 10%. The influence of radiation from impurities in the Red spectra is less significative.

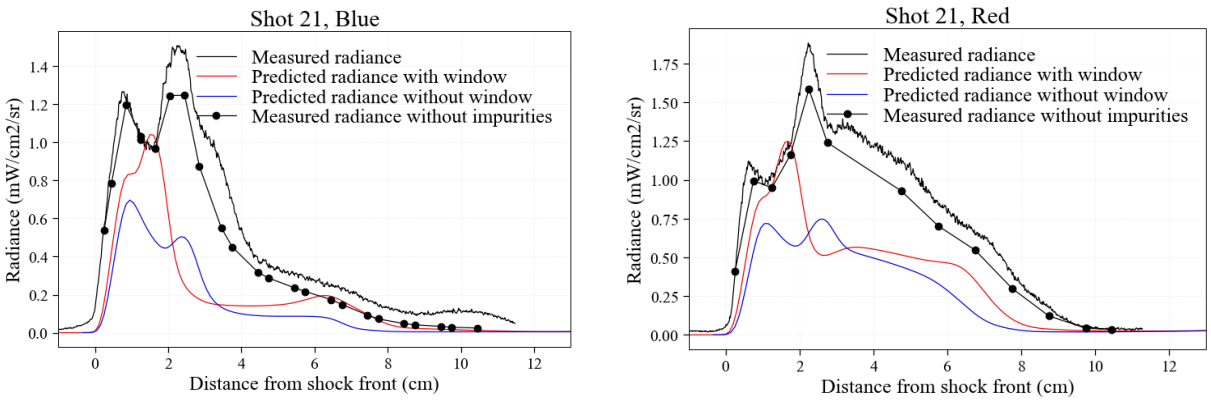

Figure 13: Comparison between predicted and experimental integrated radiance profiles for the Blue and Red cameras, including a radiance profile where all sources of radiation from impurities were removed from the experimental data.

The fitted spectra are then compared to the prediction at four chosen locations: centerline shock front, wall shock front, compression/expansion interface as predicted by CFD simulations, and the region located 10

cm from the shock front where radiation from the expanding flow is expected to be dominant. Results are given in Figure 14. In the two shock front regions, the main source of radiation comes from N_2^+ and N_2 in both the predicted and experimental results. The differences in the total spectra between simulations performed with the window and the experiments are attributed to an underprediction of N_2^+ while N_2 radiation seems to be well predicted. At the compression/expansion interface, a very good agreement is observed between the simulations with the window and the experiments, while the simulation performed without the window largely underpredicts the measured radiation. Finally, 10 cm from shock front, both simulations underpredict the measured radiation. However, most of the measured radiation (after subtraction of the CN radiation) comes from N^+. N^+ radiation is only fitted using the background radiation, and the observed lines are within the noise level. Therefore, these differences may come from a background subtraction issue during the measurements. At this point, the radiation is dominated by CN, and as observed in Figure 12, the background signal is relatively low. On the other hand, the N_2^+ radiation is relatively well predicted by the simulation performed with the window. However, N_2 radiation is underpredicted. This could come from an underprediction of N_2 by the CFD region in the expanding region coming from an error in the modelling regarding N_2 recombination, which was the goal of this test campaign. Future work will include updates in the kinetics used in the simulations to try and improve the agreement with the experiments.

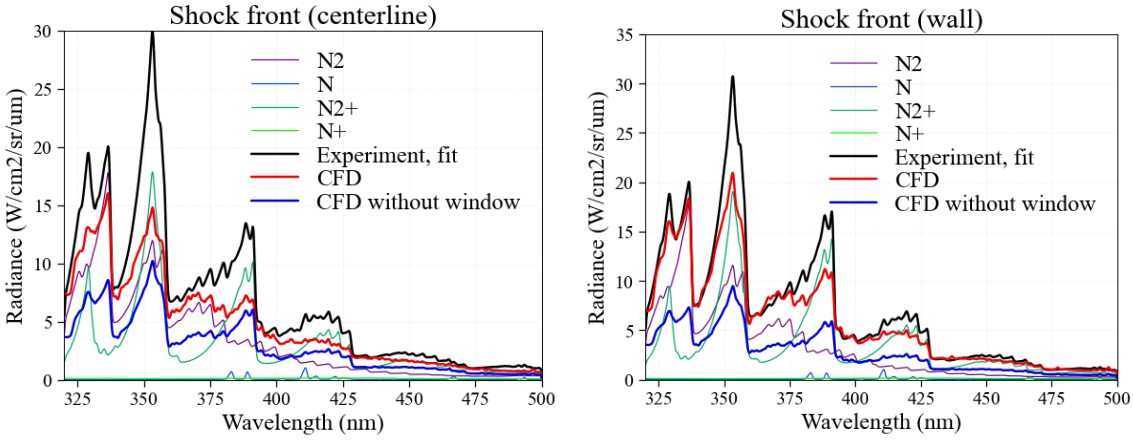

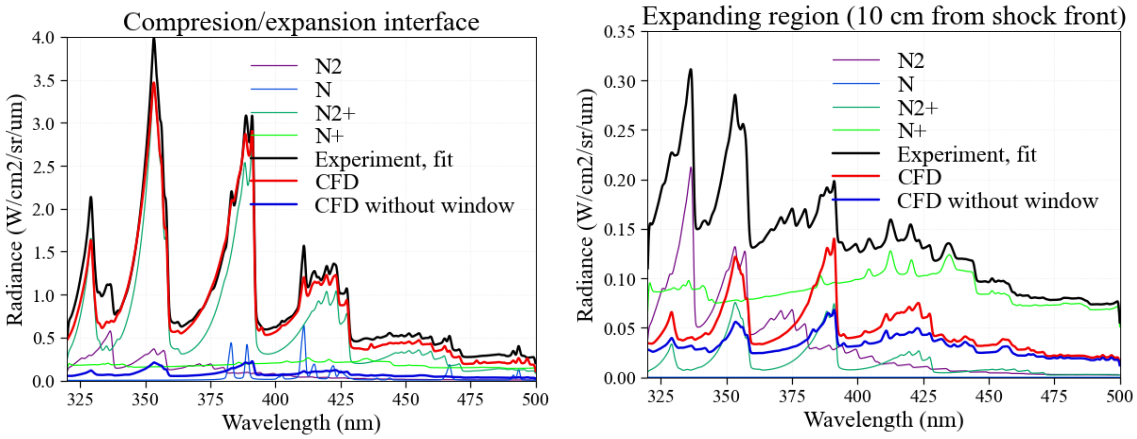

Figure 14: Comparison between predicted and experimental spectra at different axial locations. The contribution of different species is also plotted. The radiation from all impurities has been removed from the fitted spectra.

We also compared experimental and predicted temperatures. The measured temperatures are obtained by fitting the line of sight spectra. Because the multi-dimensional topology of the flow, it is not intuitively clear what these temperatures represent in physical terms. Optical emission spectroscopy will usually tend to measure the region where the gas is hotter with higher sensitivity. To study this effect, spectra, as presented in Figure 14, were reconstructed from the simulation performed with the window to mimic the spectra measured by the spectrometer. Then these reconstructed spectra were fit using NEQAIR in a similar way than as the experiments. The temperatures obtained from these fits (labeled "fit from CFD") can be compared with experiment. Results are given in Figure 15. The mean and max temperatures of the simulation across the radial position are also given for comparison. The CFD simulations aimed to reproduce shot 8 and shot 21 is also given for comparison as its velocity was relatively close to shot 8 but with a higher test time. The VUV camera was also triggered 12 μs later than the Blue camera for shot 21 and measured the same wavelength range than the Blue camera to measure radiation further away from shock front, and therefore have temperature measurements. The temperatures obtained by fitting the spectra from the CFD gives high values in the shock front region. However, for the same region in the experiments, the fit gives relatively low values. Past the shock front, the fitted temperature from CFD simulations is closer to their maximum values, even if discrepancies still remain. As a first estimation however, the experimental temperatures could be compared directly with their maximum predicted values. For shot 8, from 2 to 5 cm, the predicted temperatures seem to agree well with the experiments. This agreement is extended to 13 cm for the vibronic temperature. For shot 21, the rotational temperature obtained is consistent with shot 8. The temperatures obtained with the VUV camera are also in the continuity of those measured by the Blue camera. Note also that no significant change in the temperature slope is observed which may suggest that the driver gas has not reached the camera location, extending the test time to a maximum of 25 us. The vibrational temperature in shot 21 however seems higher than the one measured for shot 8 and the value predicted by CFD. Overall, the rotational temperature seems to be slightly overpredicted further away from

shock front, while a better agreement is observed for the vibronic temperature with shot 8, and with shot 21 after around 8 cm.

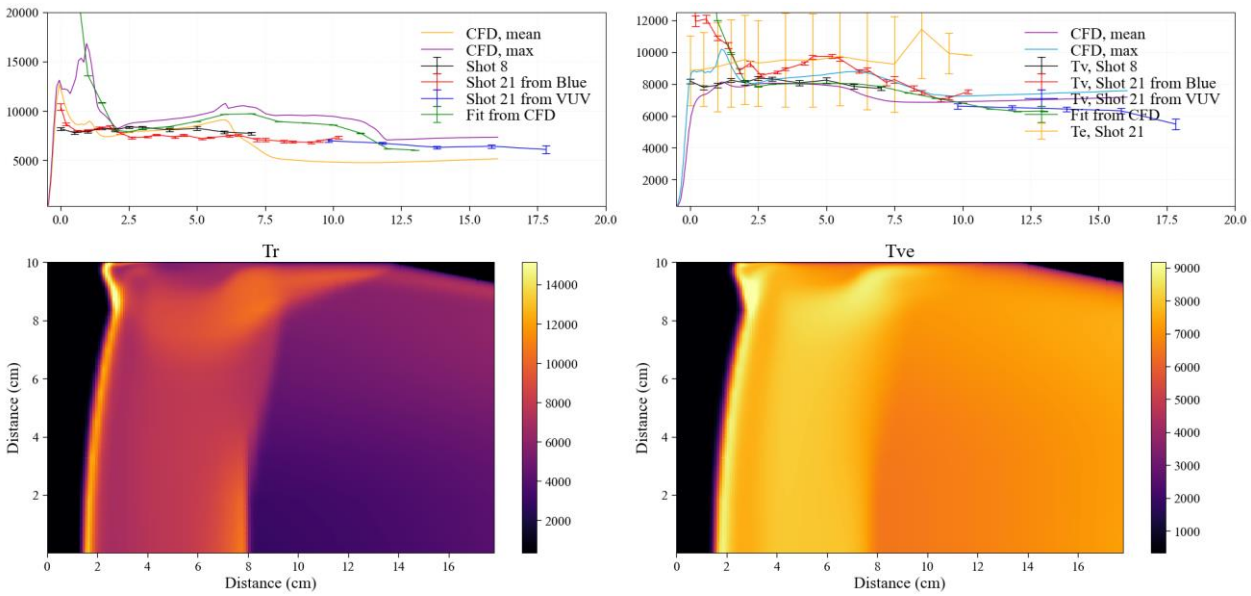

Figure 15: bottom: 2D predicted translational-rotational (right) and vibronic (left) temperature contours. Top: predicted and experimental 1D temperature profiles obtained by fitting data with NEQAIR.

Finally, the fitted spectra using NEQAIR were used to get density estimate for different species, for shots 21 and 22 representing a weakly and strongly contaminated spectra, respectively. For shot 21, both the Blue and VUV camera were used to get measurements up to 20 cm from the shock front. Results are presented in Figure 16. In the shot 21 Blue camera, the Ca^+ and Al lines almost overlaps, and the fitting procedure gave uncertainties higher than the measured density for aluminum which are therefore not shown in the figure. The VUV spectrometer measured a broader wavelength range, including an isolated aluminum line around 308 nm, which led to a more accurate estimation of aluminum densities. Aluminum lines are observed 7 cm from the shock front, but no iron lines are seen despite being included in the simulation. The results from both cameras are also consistent, and N_2 remains relatively highly populated after 20 cm. No strong slope changes are observed except from N_2 after 10 cm which could come from the expansion region. For shot 22 however, the arrival of iron lines also coincides with a depopulation of N_2 which should be expected when the driver gas arrives. Aluminum lines are also observed 1 cm before that but are then believed to come from the test gas and are not useful to determine the driver gas arrival. The densities of aluminum in shot 22 is about 10^9 cm^{-3} as it is in shot 21. This level of aluminum is therefore believed to represent only impurities present in the test gas. As stated earlier, the test time for shot 22 is then easily identified thanks to the iron lines. However, for shot 21, no iron lines or depopulation of air-based species are observed. Combined with the temperature profiles presented in Figure 15, this could suggest that the test time for that shot is much higher than the one determined via the calcium lines arrival. For future test series, a

method to experimentally determine the driver gas arrival should be implemented to get an accurate estimation of the test time.

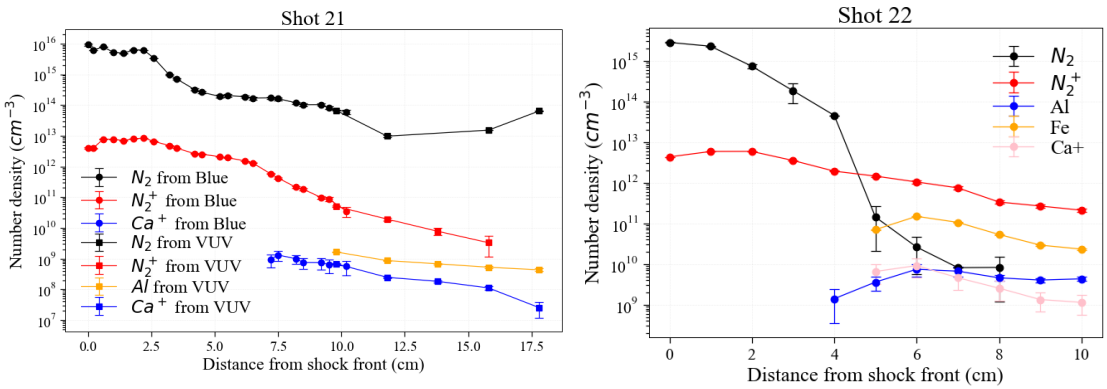

Figure 16: Number density measurements obtained by fitting the experimental spectra with NEQAIR for shot 21 and 22.

5. Conclusions

Simulations and experiments were performed in an expansion cone mounted at the end of the EAST facility. Different regions of the flow were identified: the shock front, followed by two peaks in radiation due to shock curvature, the compression/expansion interface located around 6.5 cm from the shock front, and the expanding region starting after this point.

Two different 2D simulations, referred to as with or without a window, were performed to mimic the 3D geometry of the test section. The radiation predicted by the simulation with the window generally gives better agreement with the experiments, except for the distance between the radiance intensity peaks corresponding to the centerline and wall shock front. The pitot and wall pressures are also well predicted by the simulation without the window. While it is clear that the presence of the window has a strong influence on the resulting radiation, a 3D simulation may be needed to improve the agreement with the experiments. Based on the CFD simulation, a test time of 10 to 15 μs is needed in the experiments to measure radiation from the expanding region, which represents a relatively long test time for the facility in this cone configuration. For this reason, different operating configurations were studied to improve the test time.

37 shots were performed during the test 63 experimental campaign at EAST. 16 of them were identified as providing sufficient data for further analysis. Four shots showing the best test time and data quality were also highlighted. The most important parameter for this study is the test time. However, this is not a trivial parameter to measure in the EAST facility as the driver gas arrival is not necessarily seen in the cameras. Nevertheless, lower bounds of this test time were estimated in the four highlighted shots. The maximum estimated test time was 10.5 μs in this test series but as explained in the paper, this may be underestimated.

In a future experimental campaign, an experimental method, based for instance on absorption, should be implemented to accurately detect the arrival of driver gas.

The NEQAIR radiation code was used to analyze measured radiation and compare it with CFD predictions. The total radiation was underpredicted by the CFD for the Blue and the Red cameras. This underprediction in the UV was attributed to a underprediction of N_2^+ while the underprediction of the radiation in the visible, dominated by atomic radiation, may come from a discrepancy in the temperature predictions. The temperatures being relatively well predicted, this discrepancy may be attributed to a poor prediction of number densities due to the kinetic model used. Different models should be tested or updated in a future study to improve the agreement.

Acknowledgments

Augustin Tibere-Inglesse's research was supported by an appointment to the NASA Postdoctoral Program at the NASA Ames Research Center, administered by Universities Space Research Association under contract with NASA. Khalil Bensassi, Aaron Brandis and Brett Cruden are supported by NASA contract NNA15BB15C to Analytical Mechanical Associates, Inc. This work was supported by the Entry Systems Modeling project.

References

[1] J. D. J. Anderson, "An engineering survey of radiating shock layers," *AIAA Journal,* vol. 7, no. 9, pp. 1665-1675, 1969.

[2] A. M. Brandis and B. A. Cruden, "Benchmark Shock Tube Experiments of Radiative Heating Relevant to Earth Re-entry," *American Institute of Aeronautics and Astronautics,* no. AIAA 2017-1145.

[3] C. O. Johnston and B. Kleb, "Uncertainty Analysis of Air Radiation for Lunar-Return Shock Layers," *Journal of Spacecraft and Rockets,* vol. 49, no. 3, pp. 425-434, 2012.

[4] B. A. Cruden, A. M. Brandis and C. O. Johnston, "Development of a Radiative Heating Margin Policy for Lunar Return Missions," *55th AIAA Aerospace Sciences Meeting,* no. AIAA 2017-1370, 2017.

[5] C. O. Johnston and A. M. Brandis, "Features of Afterbody Radiative Heating for Earth Entry," *Journal of Spacecraft and Rockets, Vol. 52,* vol. 52, pp. 105-119, 2015.

[6] H. Wei, R. G. Morgan, T. Mcintyre, A. M. Brandis and C. O. Johnston, "Experimental and Numerical Investigation of Air Radiation in Superorbital Expanding Flow," *American Institute of Aeronautics and Astronautics,* no. AIAA 2017-4531, 2017.

[7] A. C. Tibère-Inglesse, S. McGuire, P. Mariotto and C. O. Laux, "Validation cases for recombining nitrogen and air plasmas," *Plasma Sources Science and Technology,* vol. 27, no. 11, p. 115010, 2018.

[8] A. C. Tibère-Inglesse, "Radiation of nonequilibrium recombining plasma flows," PhD Thesis, Université Paris Saclay, 2019.

[9] B. Cruden and A. Brandis, "Measurement and Prediction of Radiative Non-equilibrium for Air Shocks Between 7-9 km/s," *47th AIAA Thermophysics Conference, Denver, CO,* Vols. AIAA 2017-4535, 2017.

[10] A. M. Brandis, C. O. Johnston, B. A. Cruden and D. K. Prabhu, "Equilibrium Radiative Heating from 9.5 to 15.5 km/s for Earth Atmospheric Entry," *Journal of Thermophysics and Heat Transfer,* vol. 31, no. 1, pp. 178-192, 2016.

[11] A. M. Brandis and B. A. Cruden, "Shock Tube Radiation Measurements in Nitrogen," *American Institute of Aeronautics and Astronautics,* no. AIAA 2018-3437, 2018.

[12] B. Cruden, R. Martinez, J. Grinstead and J. Olejniczak, "Simultaneous Vacuum-Ultraviolet Through Near-IR Absolute Radiation Measurement with Spatiotemporal Resolution in An Electric Arc Shock Tube," *41st AIAA Thermophysics Conference,* Vols. AIAA 2009-4240, AIAA, San Antonio, TX, 2009.

[13] S. P. Sharma and C. Park, "Operating Characteristics of a 60- and 10-cm Electric Arc-Driven Shock Tube-Part 11: The Driven Section," *Journal of Thermophysics and Heat Transfer,* vol. 4, no. 3, pp. 266-272, 1990.

[14] B. A. Cruden, "Absolute Radiation Measurements in Earth and Mars Entry Conditions," *Radiation and Gas-Surface Inter- action Phenomena in High-Speed Re-Entry, Von Karman Institute Lecture Series,* 2014.

[15] R. E. Dannenberg, "A conical arc driver for high-energy test facilities.," *AIAA Journal,* vol. 10, no. 12, pp. 1692-1694, 1972.

[16] R. E. Dannenberg and A. F. Silva, "Arc Driver Operation for Either Efficient Energy Transfer or High-Current Generation," *AIAA Journal,* vol. 10, no. 12, pp. 1563-1564, 1972.

[17] D. W. Bogdanoff and B. A. Cruden, "Optimizing Facility Configurations and Operating Conditions for Improved Performance in the NASA Ames 24 Inch Shock Tube," NASA technical report, 2016.

[18] E. Whiting, C. Park, L. Yen, J. Arnold and J. Paterson, "NEQAIR96,Nonequilibrium and Equilibrium Radiative Transport and Spectra Program: User's Manual," Technical Report NASA RP-1389, Ames Research Center, Moffett Field, 1996.

[19] B. A. Cruden and A. M. Brandis, "Analysis of Shockwave Radiation Data in Nitrogen," *AIAA Aviation 2019 Forum,* no. AIAA 2019-3359, 2019.

[20] A. Lani, T. Quintino, D. Kimpe and H. Deconinck, "The coolfuid framework - design solutions for high-performance object oriented scientic computing software," in *International Conference Computational Science 2005, volume 1*, Atlanta, Springer-Verlag, 2005, pp. 281-286.

[21] M. Liou and C. Steffen, "A New Flux Splitting Scheme," *Journal of Computational Physics,* vol. 107, pp. 23-39, 1993.

[22] S. Venkateswaran and C. L. Merkle, "Analysis of preconditioning methods for the Euler and Navier-Stokes equations," in *VKI LS 1999-03*, von Karman Institute for Fluid Dynamics, St.-Genesius-Rode, Belgium, March 1999.

[23] A. Lani, N. Villedieu, K. Bensassi, L. Kapa, M. Panesi and M. S. Yalim, "COOLFluiD: an open computational platform for multi-physics simulation," *21st AIAA CFD Conference,* no. AIAA 2013-2589, June 2013.

[24] K. Bensassi, A. Lani and P. Rambaud, "Unsteady simulation of hypersonic fow around a heat fux probe in ground testing conditions," *International Journal of Heat and Mass Transfer,* vol. 113, pp. 889 -897, 2017.

[25] N. A. Wright and C. A. Winkler, "Active Nitrogen," in *Physical Chemistry, A Series of Monographs*, New York, Academic Press, 1968, p. 602.